Article

Discovery Medicine 2025; 37(203): 2907–2922
https://doi.org/10.24976/Discov.Med.202537203.243

Exploring the Effects of Maslinic Acid on Gallstone Formation and Liver Injury via the PPAR Signaling Pathway

Shuo Feng[1,2,†], Zhenghao Huang[1,2,†], Fenghe Hang[1,2], Chao Shi[1,2], Dongxu Lu[1,2], Haoran Ding[1,2], Tianming Liu[1,2], Liwei Liu[1,2,*], Xianzhi Meng[1,2,*]

[1]Department of General Surgery, The First Affiliated Hospital of Harbin Medical University, 150001 Harbin, Heilongjiang, China
[2]Key Laboratory of Hepatosplenic Surgery, Ministry of Education, The First Affiliated Hospital of Harbin Medical University, 150001 Harbin, Heilongjiang, China
*Correspondence: 18940835066@163.com (Liwei Liu); mengxianzhi@hrbmu.edu.cn (Xianzhi Meng)
[†]These authors contributed equally.
Submitted: 28 August 2025 Revised: 11 October 2025 Accepted: 21 October 2025 Published: 20 December 2025

Background: Maslinic acid (MA), a pentacyclic triterpenoid found in plants, has beneficial effects at low doses, but its impact on liver damage and cholesterol gallstone (CGS) formation at high doses remains unclear. This study explored the effects of high-dose MA on liver damage and CGS formation in C57BL/6J mice.

Methods: This study used animal model experiments, network pharmacology, RNA transcriptome sequencing, molecular docking, and molecular dynamics simulation to explore the molecular mechanism by which high-dose MA promotes CGS formation and cholestatic liver injury (CLI).

Results: High-dose MA significantly promoted CGS formation ($p < 0.05$) and induced CLI in mice fed a lithogenic diet. Gallstone severity progressed with MA administration, accompanied by significant alterations in biliary lipid composition: increased cholesterol levels alongside decreased phospholipid and bile acid concentrations ($p < 0.05$), collectively leading to an elevated cholesterol saturation index (CSI, $p < 0.05$). Serum biochemical analysis confirmed hepatobiliary injury, showing significantly elevated levels of alanine aminotransferase (ALT), aspartate aminotransferase (AST), alkaline phosphatase (ALP), and total bile acids ($p < 0.05$). Histopathological examination revealed hepatic inflammatory infiltration and structural damage. Mechanistically, MA downregulated key proteins involved in bile acid synthesis and biliary excretion, while modulating regulators of cholesterol and drug metabolism. Transcriptomic profiling revealed that MA significantly disrupted pathways related to bile acid, cholesterol, and drug metabolism, particularly the Peroxisome Proliferator-Activated Receptor (PPAR) signaling pathway and bile secretion. Integrated network pharmacology, molecular docking, and dynamics simulations identified PPARα and PPARγ as core targets, with MA showing stable binding to multiple gallstone-related proteins. Subsequent validation confirmed that MA increased PPARα expression and decreased PPARγ expression ($p < 0.05$), supporting the conclusion that MA promotes gallstone formation by interfering with the PPAR signaling pathway and bile acid homeostasis.

Conclusion: Our findings indicate that high-dose MA promotes CGS formation via the PPAR signaling pathway, highlighting the potential risks of MA-induced CLI and providing a basis for assessing its safety and developing targeted interventions.

Keywords: maslinic acid; gallstone; cholestatic liver injury; bile acid metabolism; PPAR signaling pathway

Introduction

Gallstone disease (GD) represents a prevalent gastrointestinal disorder, affecting approximately one-fifth of the adult population globally, largely due to shifts in dietary patterns [1]. Gallstones are traditionally categorized into cholesterol stones, calcium bilirubinate pigment stones, brown pigment stones, and mixed-type stones, based on their distinct chemical compositions. Among these categories, cholesterol gallstones (CGS) occur most frequently [2]. Cholesterol stones can lead to complications such as biliary colic, acute cholecystitis, and pancreatitis [3]. Therefore, preventing CGS formation is of significant clinical importance.

Traditional herbal preparations are gaining widespread popularity; however, their adverse effects, particularly hepatotoxicity, are frequently underestimated [4]. Paradoxically, many herbal products, including complex formulations, single herbs, and isolated bioactive compounds, display hepatoprotective properties at low doses but can induce hepatotoxicity when exceeding certain dosage thresholds [5–7].

Maslinic acid (MA) is a naturally occurring oleanane-type pentacyclic triterpenoid, abundantly present in plants

such as mustard, basil, and hawthorn, with notably high concentrations present in olive skin [8]. Olives and olive oil, staple components of the Mediterranean diet, are well recognized for their beneficial effects in preventing chronic diseases. Consuming approximately 40 g (about 10 medium-sized olives) daily provides around 28 mg of MA.

Recent studies have reported various bioactivities of MA at low doses, including anti-tumor, anti-inflammatory, anti-malarial, and hepatoprotective effects [9–12]. However, its potential role in CGS formation and hepatotoxicity at higher doses remains unclear. Other oleanane-type triterpenoids, such as oleanolic acid and lantadene A, have been documented to induce cholestatic liver injury (CLI) when administered at high doses [13,14], and cholestasis is known to further promote gallstone formation [15].

Previous studies have shown that oral administration of 50 mg/kg/day MA to adult male Swiss CD-1 mice for 28 consecutive days did not cause hepatotoxicity [16]. However, the potential hepatotoxicity of higher doses of MA, especially when combined with a high-cholesterol diet, remains poorly understood. Additionally, the effects of elevated MA doses on CGS formation and its relationship with CLI have not been comprehensively studied. Given these knowledge gaps, the aim of this study was to investigate the hepatotoxicity of high doses of MA (200 and 400 mg/kg/day) administered via intragastric gavage and to assess the impact of these doses on CGS formation and the potential mechanisms underlying CLI in C57BL/6J mice over 28 days.

Materials and Methods

Animal Experiments

Six- to eight-week-old male C57BL/6J mice (20–22 g) were purchased from Liaoning Changsheng Biotechnology Co., Ltd. (Benxi, China) and maintained under specific pathogen-free (SPF) conditions (22 °C, 12 h light/dark cycle) with *ad libitum* access to food and water.

To establish the CGS mouse model, animals were fed for a period of four weeks with either a normal diet containing 0.02% cholesterol (ND group) or a lithogenic diet enriched with 1.25% cholesterol, 15% fat, and 0.5% cholic acid (LD group) [17]. The successful establishment of the CGS model was confirmed by visual inspection of the gallbladder, which revealed the presence of cholesterol gallstones. Biochemical analyses, including elevated total cholesterol levels in serum and bile, were also employed to validate the model.

After the dietary intervention, forty mice were randomly divided into four groups:

ND group: Mice were fed with the control diet (0.02% cholesterol) and received vehicle treatment (200 µL of 1% carboxymethylcellulose, CMC) via oral gavage for four weeks.

LD group: Mice were fed with the lithogenic diet (1.25% cholesterol, 15% fat, and 0.5% cholic acid) and received vehicle treatment (200 µL of 1% CMC) via oral gavage for four weeks.

MA-L group (low-dose maslinic acid group, LD + 200 mg/kg MA): Mice were fed with the lithogenic diet and received a low dose of MA (200 mg/kg/day) via oral gavage for four weeks.

MA-H group (high-dose maslinic acid group, LD + 400 mg/kg MA): Mice were fed with the lithogenic diet and received a high dose of MA (400 mg/kg/day) via oral gavage for four weeks.

After a one-week dietary adaptation period, all groups were treated accordingly. ND and LD groups received 1% CMC as a vehicle control, while the MA-L and MA-H groups were administered the respective MA doses.

Mice were euthanized at the end of the experimental period in accordance with the Guide for the Care and Use of Laboratory Animals and institutional ethical approval. Deep anesthesia was induced and maintained using a precision vaporizer (R500, RWD Life Science, Shenzhen, China) delivering isoflurane (R510-22-10, RWD Life Science, Shenzhen, China, 4% induction, 1.5% maintenance). Once the absence of pedal reflexes was confirmed, euthanasia was performed by cervical dislocation to ensure a rapid and humane death, minimizing pain and distress.

Bile and Serum Collection

After anesthesia, the gallbladder was carefully excised, and the bile was drained by cutting open the gallbladder. The collected bile was then centrifuged at 1500 $\times g$ for 10 minutes at 4 °C, and the supernatant was stored at –80 °C for further analysis. Blood was collected by cardiac puncture under deep anesthesia. The blood was drawn into sterile tubes, allowed to clot at room temperature for 30 minutes, and serum was separated by centrifugation at 1500 $\times g$ for 10 minutes at 4 °C. The serum was then stored at –80 °C until analysis.

Biochemical Analyses of the Bile and Serum Samples

Commercially available colorimetric assay kits for alanine aminotransferase (ALT; Catalog # C009-1-1), aspartate aminotransferase (AST; Catalog # C010-1-1), alkaline phosphatase (ALP; Catalog # A059-2-2), total cholesterol (TC; Catalog # A111-1-1), and total bile acids (TBA; Catalog # E003-2-1) were purchased from Nanjing Jiancheng Bioengineering Institute (Nanjing, China). These kits were employed to measure the aforementioned biochemical parameters in serum and bile, in strict adherence to manufacturers' instructions. Phospholipid concentrations were determined using a dedicated assay kit (Catalog # 295-94401, Wako Pure Chemicals, Osaka, Japan) following recommended procedures. Absorbance values for all biochemical measurements were obtained using a BioTek Synergy NEO multi-mode microplate reader (BioTek Instruments, Winooski, VT, USA).

Histopathology

After deep anesthesia, a midline incision was made in the animals to expose the liver. Liver tissue samples were carefully excised, ensuring no contamination from other organs. The samples were immediately fixed in 4% paraformaldehyde, followed by conventional embedding in paraffin wax. Sections measuring approximately 3.5 µm thick were accurately prepared using a Leica RM2245 microtome (Leica Biosystems, Nussloch, Germany). These sections underwent routine processes of deparaffinization, rehydration, and staining with hematoxylin and eosin (Catalog # G1120, Solarbio, Beijing, China).

Western Blot

Protein samples were subjected to electrophoretic separation using 10% sodium dodecyl sulfate polyacrylamide gel electrophoresis (SDS-PAGE) gels (Catalog # P1200-1, Solarbio, Beijing, China), followed by transfer onto polyvinylidene difluoride (PVDF) membranes (Millipore, Burlington, MA, USA). The membranes were then subjected to blocking with 5% (w/v) non-fat dry milk in Tris-Buffered Saline with Tween-20 (TBST, 20 mM Tris-HCl, pH 7.5, 150 mM NaCl, 0.1% Tween-20) for 1 h at room temperature. Primary antibodies were applied overnight at 4 °C, including anti-cholesterol 7α-hydroxylase (CYP7A1, Catalog # ab65596, Abcam, Cambridge, UK; dilution 1:1000), anti-cholesterol 12α-hydroxylase (CYP8B1, Catalog # ab191910, Abcam, Cambridge, UK; dilution 1:1000), anti-cholesterol 27-hydroxylase (CYP27A1, Catalog # ab227248, Abcam, Cambridge, UK; dilution 1:1000), anti-ATP-binding cassette sub-family B member 4 (ABCB4, Catalog # ab317573, Abcam, Cambridge, UK; dilution 1:1000), anti-ATP-binding cassette sub-family G member 5 (ABCG5, Catalog # 27722-1-AP, Proteintech, Wuhan, China; dilution 1:1000), anti-bile salt export pump (BSEP, Catalog # 67512-1-Ig, Proteintech, Wuhan, China; dilution 1:5000), anti-sterol O-acyltransferase 2 (SOAT2, Catalog # PA5-100373, Thermo Fisher Scientific, Waltham, MA, USA; dilution 1:1000), anti-3-hydroxy-3-methylglutaryl-CoA reductase (HMGCR, Catalog # PA5-37367, Thermo Fisher Scientific, Waltham, MA, USA; dilution 1:1000), anti-Proprotein convertase subtilisin/kexin type 9 (PCSK9, Catalog # 27882-1-AP, Proteintech, Wuhan, China; dilution 1:1000), anti-cytochrome P450 2B10 (CYP2B10, Catalog # AB9916, Merck, Darmstadt, Germany; dilution 1:5000), anti-Peroxisome proliferator-activated receptor alpha (PPARα, Catalog # ab126285, Abcam, Cambridge, UK; dilution 1:1000), anti-Peroxisome proliferator-activated receptor gamma (PPARγ, Catalog # 16643-1-AP, Proteintech, Wuhan, China; dilution 1:1000), and anti-glyceraldehyde-3-phosphate dehydrogenase (GAPDH, Catalog # 60004-1-Ig, Proteintech, Wuhan, China; dilution 1:50,000).

Membranes were then incubated with secondary antibodies conjugated with HRP (Goat Anti-Mouse IgG, Catalog # SA00001-1, Proteintech, Wuhan, China; dilution 1:2000; Goat Anti-Rabbit IgG, Catalog # SA00001-2, Proteintech, Wuhan, China; dilution 1:2000). Enhanced chemiluminescence (ECL) reagent (Catalog # BL520A, Biosharp, Hefei, China) was used to detect and visualize protein bands.

The grayscale values of the protein bands were measured using ImageJ software (version 1.53, National Institutes of Health, Bethesda, MD, USA). The relative expression of each protein was calculated by normalizing the band intensity to the GAPDH control. Quantification was performed by determining the integrated density of each band, and statistical analysis of protein expression was conducted using GraphPad Prism (version 9.0, GraphPad Software, San Diego, CA, USA).

RNA Sequencing

Liver samples were randomly harvested from three mice in each experimental group (LD and MA-H) after partial hepatectomy for RNA sequencing (RNA-seq) analysis performed by Shanghai LingEn Biotechnology Co., Ltd. (Shanghai, China). Total RNA was extracted utilizing Trizol reagent (Catalog # 15596026, Invitrogen, Carlsbad, CA, USA), precisely following the guidelines provided by the manufacturer. The extracted RNA samples were then dissolved in 50 µL RNase-free DEPC water (Catalog # AM9920, Ambion, Austin, TX, USA). Purity and integrity of the RNA samples were confirmed using a Qubit 4.0 fluorometer (Thermo Fisher Scientific, Waltham, MA, USA) and a Qsep400 analyzer (Catalog # Qsep400, BiOptic, Taipei, Taiwan), respectively. After initial quality trimming of raw sequencing data using the FASTP tool (version 0.20.1, Open Source, Shenzhen, China), gene expression quantification was performed by featureCounts (version 2.0.3, Subread package, Walter and Eliza Hall Institute of Medical Research, Melbourne, VIC, Australia), and normalized values were presented as fragments per kilobase of transcript per million mapped reads (FPKM), ensuring accurate normalization based on transcript length and sequencing depth.

Functional Enrichment Analysis of CGS Pathogenesis

To investigate the underlying mechanisms of CGS development, integrated bioinformatics analyses, including Gene Ontology (GO), Kyoto Encyclopedia of Genes and Genomes (KEGG), and Gene Set Enrichment Analysis (GSEA), were performed. GO terms were classified into three categories: biological processes (BP), cellular components (CC), and molecular functions (MF). The KEGG database identified significant modifications in pathways associated with lipid metabolism and inflammatory processes. Furthermore, GSEA was employed to explore subtle yet biologically meaningful changes in gene expression. Final pathway representations were visualized through the Bioinformatics Platform.

Construction of Protein–Protein Interaction Network

To construct a protein-protein interaction (PPI) network, potential targets of MA were first identified using the SwissTargetPrediction database and the Comparative Toxicogenomics Database. Gallstone-associated genes were retrieved from GeneCards. Overlapping genes between MA-associated targets and gallstone-related genes were identified as candidate targets involved in MA-induced gallstone formation.

Using the STRING database [18], a PPI network comprising overlapping targets was constructed and graphically represented using Cytoscape software (version 3.9.1, Cytoscape Consortium, San Diego, CA, USA) [19]. Topological metrics such as betweenness centrality and eigenvector centrality were analyzed through the CytoNCA plugin (version 2.1.6, National Center for Protein Sciences, Beijing, China; available from the Cytoscape App Store) [20]. Targets exceeding mean values across all four metrics were deemed critical, and intersections among these significant targets were identified to elucidate essential mediators potentially underlying gallstone formation induced by MA.

Molecular Docking

The two-dimensional (2D) structure of MA was obtained from PubChem and optimized to a three-dimensional (3D) conformation with minimal free energy using Chem3D (version 20.0, PerkinElmer, Waltham, MA, USA). Structural preprocessing was conducted using PyMOL molecular visualization software (version 2.5.0, Schrödinger, LLC, New York, NY, USA) and included: (1) removal of co-crystallized ligands, and (2) removal of water molecules from crystal structures. This preparation yielded clean receptor structures suitable for molecular docking.

AutoDock Tools (version 1.5.6, The Scripps Research Institute, La Jolla, CA, USA) was used to convert receptor and ligand structures into PDBQT format and to define docking grid box parameters. The predicted binding poses and interaction sites were visualized using PyMOL (https://www.pymol.org/).

Molecular Dynamics Simulation

Molecular dynamics (MD) simulations were carried out with the GROMACS 2022 software package (http://www.gromacs.org/). Initial ligand-protein docking structures were solvated within TIP3P water boxes (version 36, CHARMM, Cambridge, MA, USA), ensuring a minimum 1 nm boundary distance, and subsequently neutralized with counterions (Na^+/Cl^-) [21]. Force-field parameters for proteins and ligands were obtained from the CHARMM36 force field (version 36, Chemistry at HARvard Macromolecular Mechanics, Cambridge, MA, USA) and the CGenFF generator (version 3.0.1, MacKerell Lab, University of Maryland, Baltimore, MD, USA) [22]. Energy minimization processes involved three consecutive steps, after which the systems were equilibrated under NVT and NPT ensembles at 310 K. Following equilibration, MD simulations were performed for 100 ns with a time-step of 2 fs. Root mean square deviation (RMSD) and root mean square fluctuation (RMSF) calculations were conducted to evaluate structural stability and flexibility. Additional metrics, including radius of gyration (Rg) and solvent-accessible surface area (SASA), were used to evaluate protein compactness and solvent exposure. Long-range electrostatic interactions were treated using the Particle Mesh Ewald (PME) method with a 1 nm cutoff. Binding free energies were estimated by MM-PBSA calculations via the gmx_MMPBSA tool (version 1.1, part of the GROMACS–MMPBSA package, University of Valencia, Valencia, Spain).

Statistical Analysis

Data were analyzed using one-way analysis of variance (ANOVA) followed by Tukey's post-hoc test for multiple comparisons, with results presented as mean ± standard deviation (SD). Statistical tests and graphical representations were generated using GraphPad Prism (version 8.0.1, GraphPad Software, San Diego, CA, USA). A $p < 0.05$ was considered statistically significant.

Results

MA Promotes CGS Formation in Mice

This study evaluated the impact of MA on CGS formation in mice fed a high-cholesterol diet. Animals were divided into four groups (ND, LD, MA-L, and MA-H), with the dosing regimen illustrated in Fig. 1A. All mice in the LD group developed gallstones, with the majority classified as stages II–III according to established grading criteria [23]. MA treatment significantly exacerbated gallstone severity: the MA-L group exhibited an average gallstone stage of III, while the MA-H group showed more severe lesions, averaging stage IV. These results indicate that MA administration increased gallstone severity ($p < 0.05$, Fig. 1B,C).

The cholesterol saturation index (CSI) was calculated based on Carey's established method [24]. As shown in Fig. 1D, CSI values were significantly elevated in the LD group compared with the ND group ($p < 0.05$). Moreover, both MA-L and MA-H groups exhibited further increases in CSI compared to the LD group ($p < 0.05$). Fig. 1E demonstrates that biliary cholesterol content was markedly higher in the LD group than in the ND group ($p < 0.05$), whereas no significant differences were observed between the LD group and either MA-treated group (MA-L or MA-H, $p > 0.05$).

As shown in Fig. 1F, total bile acid levels did not differ significantly between the ND and LD groups ($p > 0.05$). However, both MA-L and MA-H groups showed significant reductions in bile acid levels compared to the LD group ($p < 0.05$). Similarly, phospholipid concentrations were comparable between the ND and LD groups ($p > 0.05$),

but were significantly decreased in the MA-L and MA-H groups ($p < 0.05$, Fig. 1G).

In summary, the elevated CSI in the LD group compared to the ND group was primarily attributable to increased biliary cholesterol content. In contrast, the further rise in CSI in MA-treated groups compared to the LD group appeared to be driven by reductions in bile acid and phospholipid concentrations, while cholesterol levels remained unchanged. Collectively, these *in vivo* findings demonstrate that MA promotes CGS formation in mice fed a high-cholesterol diet.

High-Dose MA Induces CLI in Mice

Consistent with previously reported effects of high-dose oleanolic acid [25], MA—another oleanane-type pentacyclic triterpenoid—was found to induce liver injury at elevated doses. Analysis of serum biochemical parameters revealed that MA administration resulted in an increase in serum ALT and AST levels ($p < 0.05$, Fig. 2A,B), indicating hepatocellular injury and cell death. Similarly, serum ALP levels rose with MA administration ($p < 0.05$, Fig. 2C), suggesting that CLI may be one mechanism through which high-dose MA promotes CGS formation.

Furthermore, analysis showed that serum total bile acid (TBA) levels in the LD group were significantly elevated compared to the ND group ($p < 0.05$). Moreover, both low- and high-dose MA treatment further increased TBA concentrations relative to the LD group ($p < 0.05$, Fig. 2D).

Histological examination provided further evidence of hepatotoxicity in the high-dose MA group, showing disrupted hepatic architecture, marked inflammatory cell infiltration around portal areas, erythrocyte extravasation, blurred hepatic cord structures, and focal hepatocyte lysis with loss of nucleoli (Fig. 2E). Together, these findings substantiate that high-dose MA induces CLI, supporting the proposed mechanism for its promotive effect on CGS formation.

Altered Expression of Proteins Related to Bile Acid Homeostasis in MA-Treated Mice

To elucidate the mechanisms by which MA promotes CGS formation, we examined the hepatic expression of key proteins involved in bile acid (BA) homeostasis, cholesterol transport, and metabolism.

Western blot analysis revealed that MA treatment significantly suppressed the protein expression of key enzymes in bile acid synthesis pathways, including CYP7A1 and CYP8B1, compared to the LD group ($p < 0.05$, Fig. 3A,B). While the decrease in the MA-L group was not statistically significant ($p > 0.05$), the high dose of MA (MA-H) led to a significant downregulation of CYP27A1 protein expression compared to the LD group ($p < 0.05$). This overall downregulation of BA synthetic enzymes may represent a compensatory response to elevated systemic BA levels.

Furthermore, MA administration significantly reduced the hepatic protein levels of ABCB4, a phospholipid transporter [26], and BSEP, the primary bile acid export pump [27] ($p < 0.05$, Fig. 3C,D). These findings are consistent with the observed reductions in biliary phospholipid and BA levels, suggesting that MA impairs the hepatic secretion of these critical biliary lipids. In contrast, the expression of ABCG5, a sterol transporter mediating cholesterol secretion into bile [28], was not significantly altered in the MA-L and MA-H groups compared to the LD group ($p > 0.05$).

Analysis of cholesterol metabolism-related proteins showed that MA treatment significantly upregulated the expression of HMGCR, the rate-limiting enzyme in cholesterol synthesis ($p < 0.05$), and downregulated PCSK9, a regulator of low-density lipoprotein (LDL) receptor degradation ($p < 0.05$, Fig. 3E,F). No consistent significant effect of MA was observed on SOAT2 protein expression ($p > 0.05$). Additionally, MA induced a reduction in the expression of CYP2B10, a key drug-metabolizing enzyme ($p < 0.05$), further supporting the induction of CLI by high-dose MA.

Collectively, these results demonstrate that MA promotes CGS formation through multifaceted mechanisms involving the suppression of BA synthesis, impairment of biliary phospholipid and BA secretion, promotion of hepatic cholesterol synthesis, and induction of CLI.

RNA-seq Reveals Metabolic Alterations in Mouse Liver Induced by MA

To investigate the impact of MA on hepatic metabolism, RNA-seq was performed on liver tissues from the LD and MA-H groups. Genes exhibiting significant differential expression were analyzed via KEGG and GO enrichment analyses using clusterProfiler (version 4.10.0, The University of Hong Kong, Hong Kong, China) in R. As shown in Fig. 4A, differential expression analysis revealed significant variations in genes associated with cholesterol and drug metabolism across experimental groups. GO enrichment analysis identified numerous BP linked to cholesterol regulation and xenobiotic metabolism (Fig. 4B). Additionally, KEGG pathway analysis highlighted several significantly enriched pathways, including those related to cholesterol metabolism, BA synthesis and secretion, and drug biotransformation (Fig. 4C). These data strongly corroborate our earlier observations, indicating that MA exposure promotes gallstone formation and induces CLI primarily by disrupting cholesterol and BA homeostatic mechanisms. Furthermore, the presence of differentially expressed genes in the PPAR signaling cascade suggests that MA exposure could exacerbate CGS development via interference with PPAR-mediated regulatory networks. GSEA further revealed downregulation of primary BA biosynthesis pathways in the MA-H group (Fig. 4D), suggesting a potential compensatory response to

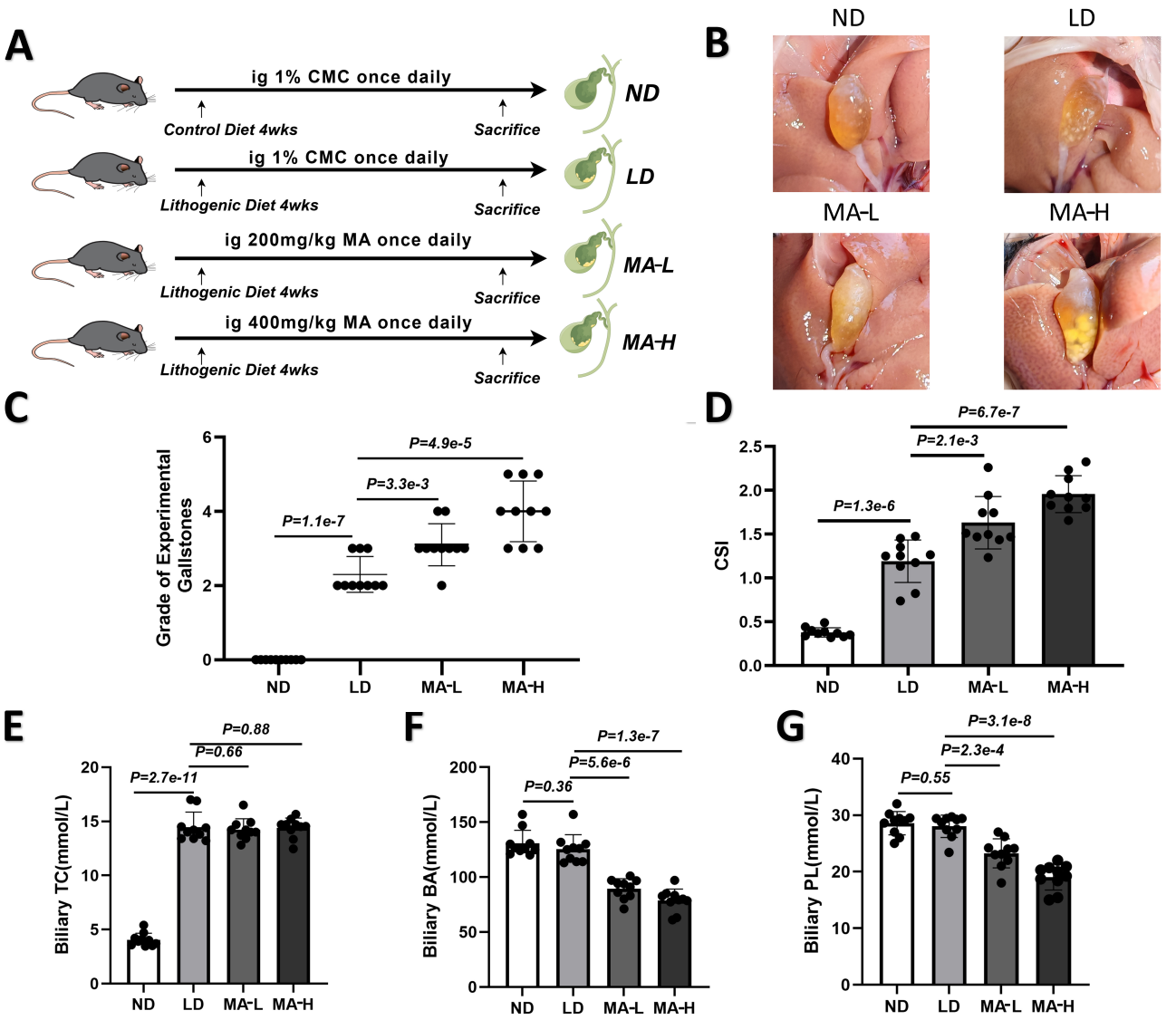

Fig. 1. High-dose maslinic acid (MA) increases gallstone formation risk under lithogenic diet (LD) conditions. (A) Schematic representation of the animal experimental protocol. (B) Representative images of gallstone morphology in experimental mouse groups. (C) Severity classification of CGS in mice. (D) Cholesterol saturation index (CSI) measurements in bile samples. (E) Content of total cholesterol (TC) in bile among different groups. (F) Content of total bile acid (BA) in bile among different groups. (G) Phospholipid (PL) content in bile among different groups. Values are presented as mean ± Standard Error of the Mean (SEM); $n = 10$ mice per group. Statistical analysis was performed using one-way analysis of variance (ANOVA) followed by Tukey's post-hoc test. Exact p-values are indicated on the graph; comparisons were made between each treatment group and the LD control group. ND, normal diet; LD, lithogenic diet; MA-L, low-dose maslinic acid group; MA-H, high-dose maslinic acid group.

BA accumulation. Pathways related to drug metabolism were also suppressed (Fig. 4E), consistent with the hepatotoxic effects observed in MA-treated mice. The observed suppression of the PPAR signaling pathway supports the hypothesis that MA promotes gallstone formation through modulation of this pathway (Fig. 4F).

Network Toxicology Identifies Mechanisms by Which MA Promotes Gallstone Formation

Network pharmacology analysis was conducted to identify potential molecular targets involved in MA-induced gallstone formation. Initially, 85 MA-associated genes were identified from the SwissTargetPrediction and Comparative Toxicogenomics Database. Concurrently, 959 CGS-related genes were obtained from the GeneCards database. A Venn diagram identified 30 overlapping genes (Fig. 5A). To further illustrate how MA influences gallstone pathogenesis at the molecular level, a PPI network was constructed using these intersecting genes. By analyzing key topological metrics, nine critical proteins were identified (Fig. 5B). Notably, PPARγ and PPARα emerged as central nodes within the network, reinforcing our hy-

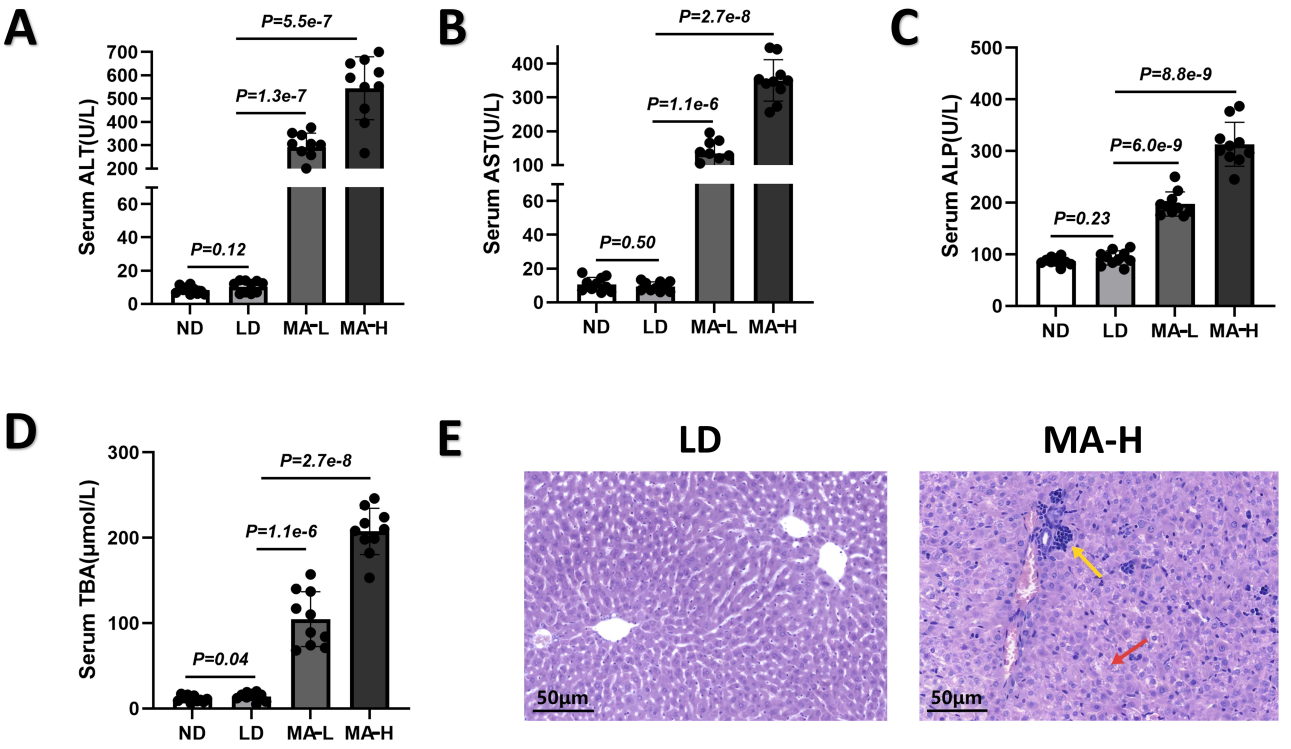

Fig. 2. Hepatotoxicity induced by high-dose MA. (A–D) Serum biochemical parameters, including alanine aminotransferase (ALT) (A), aspartate aminotransferase (AST) (B), alkaline phosphatase (ALP) (C), and total bile acid (TBA) (D). (E) Liver sections stained with hematoxylin-eosin (H&E). Yellow arrow indicates significant inflammatory cell infiltration, while red arrow indicates areas of partial hepatocyte dissolution. Data are presented as mean ± SEM; n = 10 mice per group. Statistical analysis was performed using one-way ANOVA followed by Tukey's post-hoc test. Exact p-values are shown in the figure. Comparisons were made against the LD control group. The LD group served as the baseline control for these mechanistic studies to directly evaluate the effects of MA-H treatment under gallstone-prone conditions.

pothesis regarding the pivotal role of the PPAR signaling pathway in MA-induced CGS formation. To elucidate functional implications, overlapping genes were subjected to additional GO enrichment analyses, focusing specifically on the top five enriched terms across the BP, CC, and MF categories (Fig. 5C). Key enriched biological processes included negative modulation of inflammation, inhibition of cholesterol accumulation, maintenance of cholesterol equilibrium, BA and salt transport, and cellular responses triggered by BA stimuli. Enriched cellular components included chromatin, nucleoplasm, cytosol, protein-containing complexes, and RNA polymerase II transcription regulator complexes. Molecular functions significantly enriched included identical protein binding, transcription coactivator binding, sterol binding, *cis*-regulatory region binding, and enzyme binding. Differentially expressed genes were further subjected to KEGG analysis to explore signaling pathways associated with MA-induced gallstone formation. The results specifically targeted pathways that may mediate the lithogenic effects of MA. As illustrated in Fig. 5D, these targets were predominantly enriched in the PPAR signaling pathway, bile secretion, and inflammatory pathways. Integration of core targets and pathway enrichment results highlighted the critical involvement of PPAR signaling in MA-induced gallstone formation.

Molecular Docking Analysis

Binding patterns and affinities of MA toward CGS-associated targets were examined via molecular docking. Core MA targets related to CGS formation were selected for docking analysis. As shown in Fig. 6, all nine target proteins were predicted to spontaneously interact with MA, suggesting targets such as PPARγ and PPARα are likely primary direct effectors mediating the pro-gallstone effects of MA. Docking results confirmed the predicted binding conformations of MA with these target proteins, supporting the hypothesis that MA may enhance CGS formation via direct interaction with critical regulatory proteins.

MD Simulation Analysis

The RMSD, which reflects atomic displacement during MD simulations, was used to assess system stability, with lower values implying greater structural consistency. As illustrated in Fig. 7A, the PPARα–MA complex stabilized after 5 ns and exhibited minimal fluctuations around 2.4 Å thereafter. Similarly, the PPARγ–MA com-

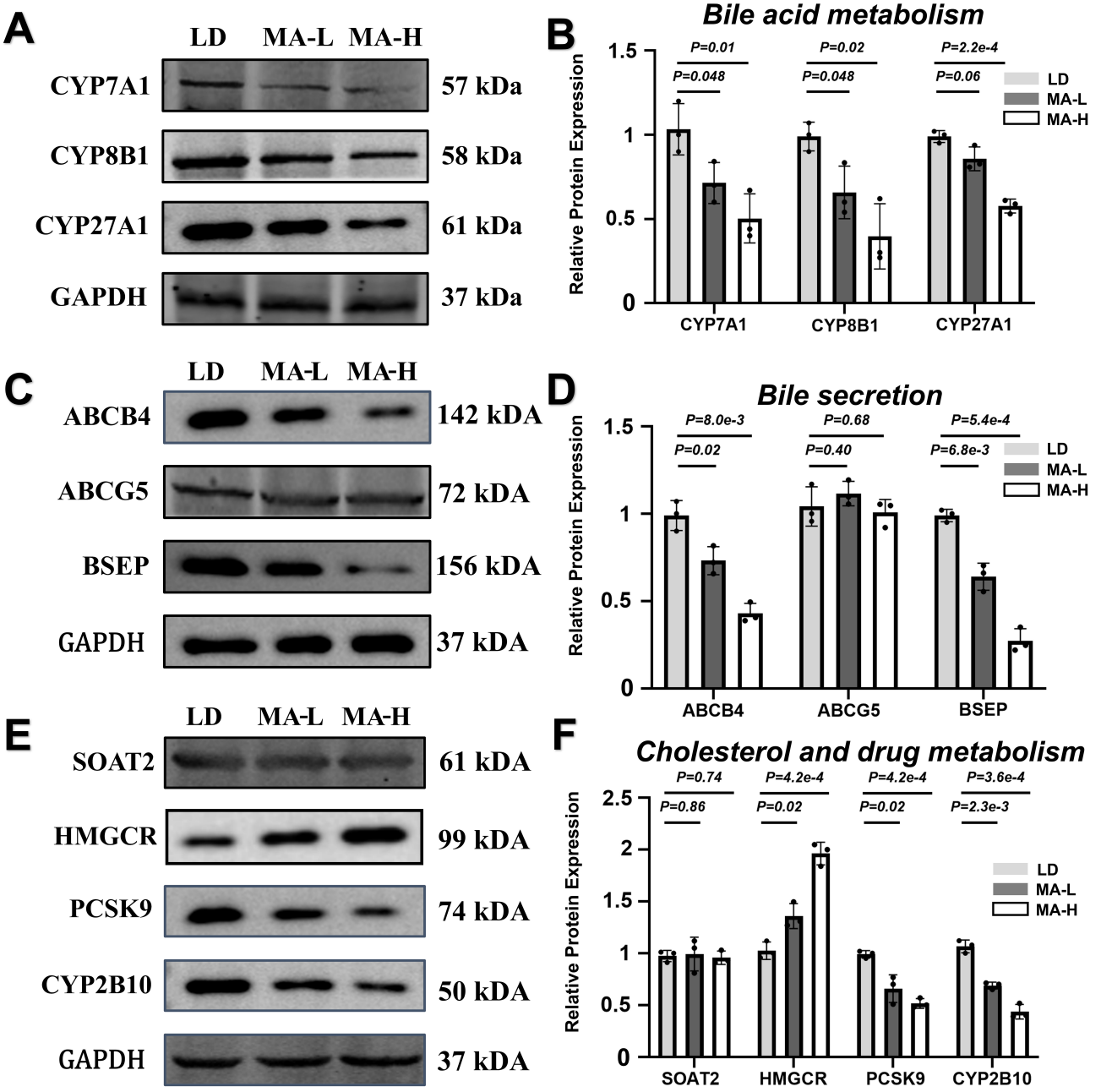

Fig. 3. Protein expression changes related to bile acid (BA) and cholesterol metabolism, bile secretion, and drug metabolism. (A) Western blot analysis of proteins involved in BA metabolism in LD, MA-L, and MA-H groups. (B) Quantitative protein expression analysis related to BA metabolism. (C) Western blot analysis of bile secretion-related proteins. (D) Quantitative comparison of proteins associated with bile secretion. (E) Western blot analysis of cholesterol and drug metabolism-related proteins. (F) Quantitative analysis of cholesterol and drug metabolism-associated protein expression. Data are presented as mean ± SEM; $n = 3$ mice per group. Statistical analysis was performed using one-way ANOVA followed by Tukey's post-hoc test. Exact p-values are indicated in the figure. Comparisons were made relative to the LD group. The LD group served as the baseline control for these mechanistic studies to directly evaluate the effects of MA treatment under gallstone-prone conditions. CYP7A1, cholesterol 7α-hydroxylase; CYP8B1, cholesterol 12α-hydroxylase; CYP27A1, cholesterol 27-hydroxylase; GAPDH, glyceraldehyde-3-phosphate dehydrogenase; ABCB4, ATP-binding cassette sub-family B member 4; ABCG5, ATP-binding cassette sub-family G member 5; BSEP, bile salt export pump; SOAT2, sterol O-acyltransferase 2; HMGCR, 3-hydroxy-3-methylglutaryl-CoA reductase; PCSK9, proprotein convertase subtilisin/kexin type 9; CYP2B10, cytochrome P450 2B10.

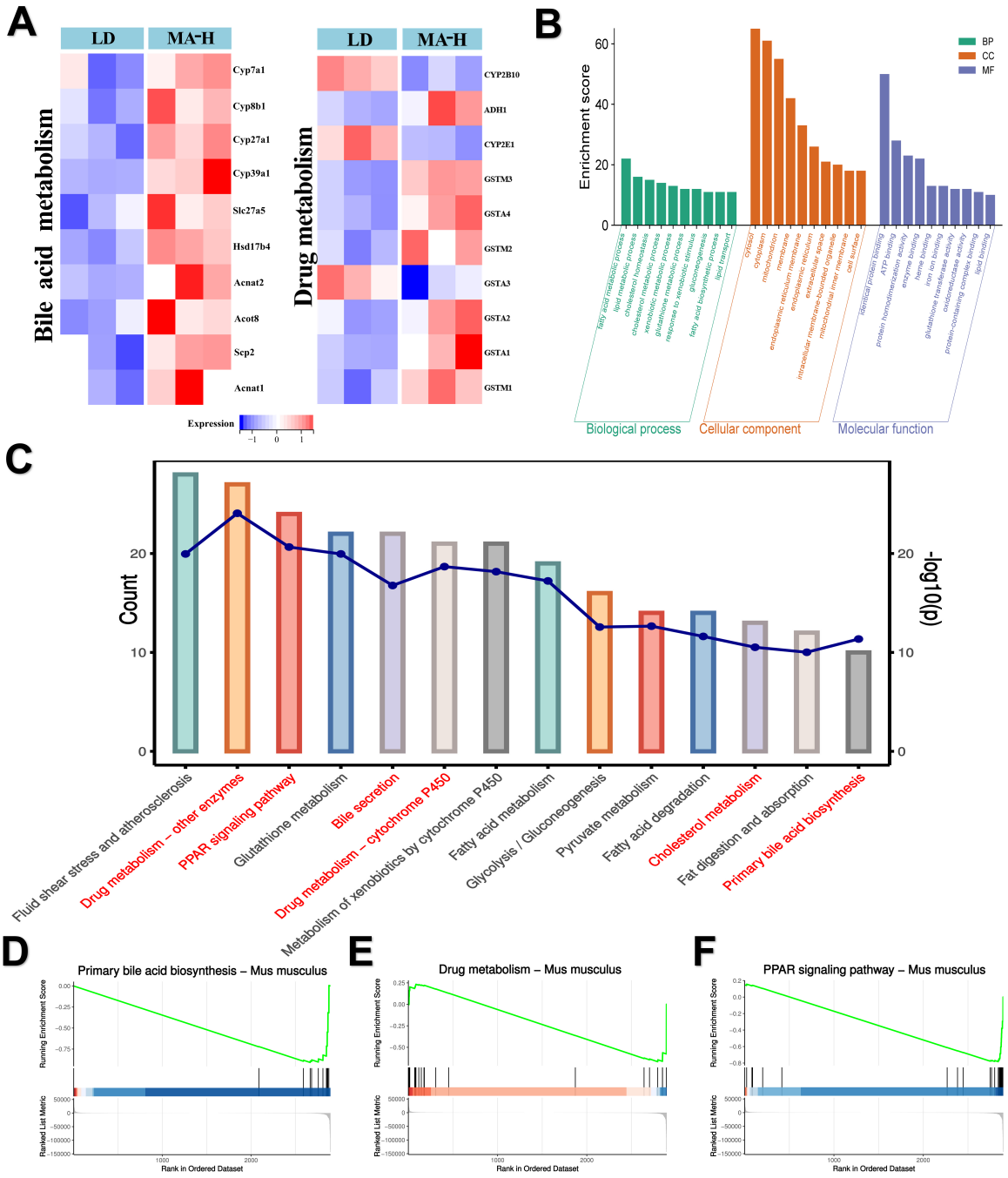

Fig. 4. Transcriptomic profiling reveals gene expression alterations in mouse liver after MA treatment. (A) Heatmap of differentially expressed genes related to BA and drug metabolism. (B) Gene Ontology (GO) enrichment analysis. (C) Kyoto Encyclopedia of Genes and Genomes (KEGG) analysis. Each bar represents the number of genes associated with each pathway, while the dark blue line indicates the –log10(p) value for each pathway. (D–F) Gene Set Enrichment Analysis (GSEA) of relevant pathways.

plex reached equilibrium at approximately 90 ns and fluctuated consistently around 2.27 Å afterward. These observations indicate that MA forms highly stable complexes with both PPARα and PPARγ.

Protein compactness was evaluated via radius of gyration (Rg) analysis, with higher values indicating expansion. The Rg analysis showed stable fluctuations for the PPARα–MA complex throughout the simulation, indicating no significant expansion or contraction. The PPARγ–MA complex displayed minor fluctuations at first and stabilized subsequently, suggesting slight conformational adjustments during the simulation (Fig. 7B). SASA values for both complexes exhibited minor fluctuations and gradually stabilized over time (Fig. 7C), suggesting ligand binding modestly alters the binding microenvironment and SASA. Ligand–protein interactions significantly depend on hydro-

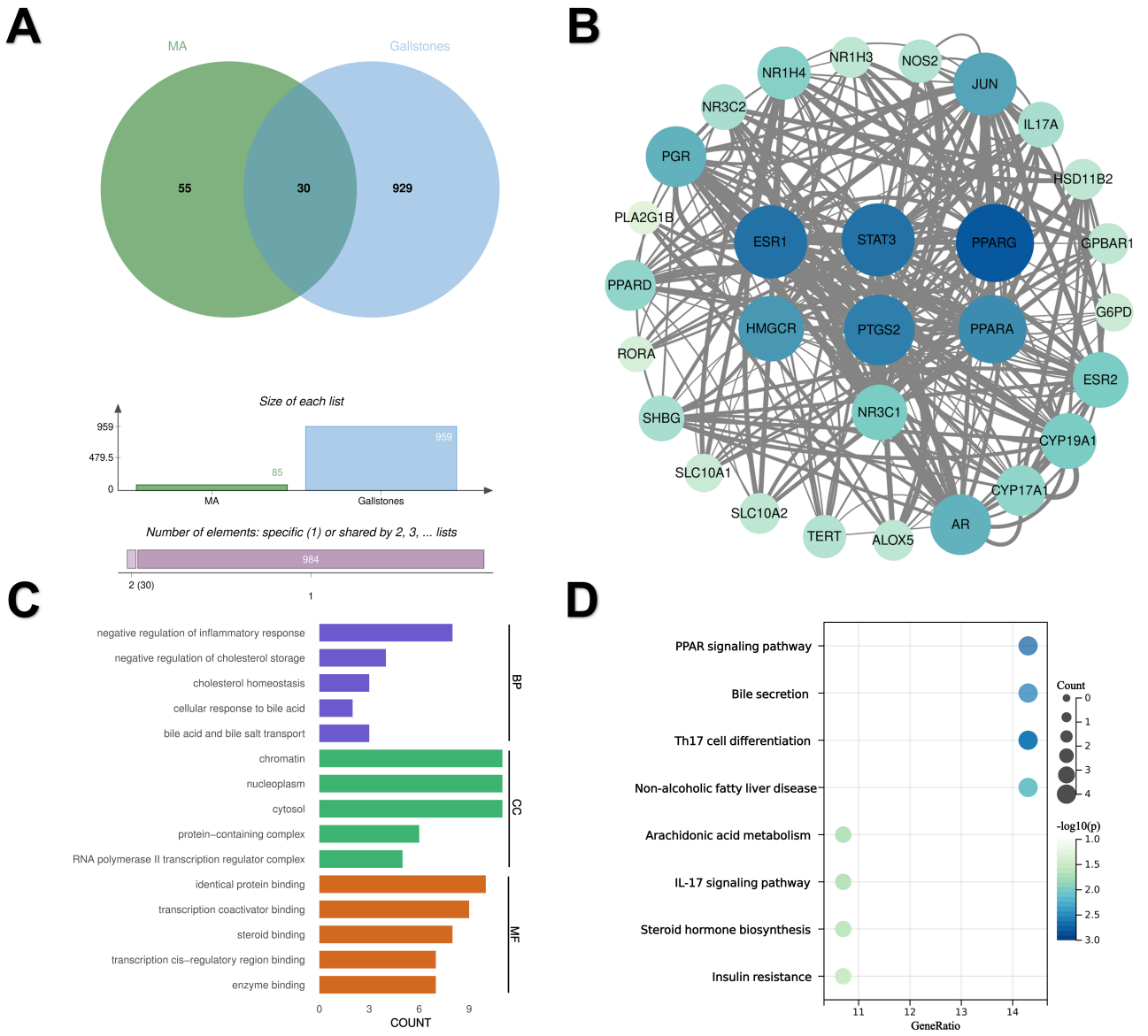

Fig. 5. Analysis of MA-associated molecular targets related to gallstone formation. (A) Venn diagram illustrating overlapping targets between MA-related and gallstone-related genes. (B) Protein-protein interaction (PPI) network showing core targets through which MA promotes gallstone formation. Node size corresponds to centrality; darker blue represents stronger associations, while lighter blue indicates weaker associations. Core targets are highlighted centrally. (C,D) Summary of highly enriched GO terms (top 15 in biological processes [BP], cellular components [CC], molecular functions [MF] categories) and KEGG pathway enrichment analysis results.

gen bonds. Fig. 7D illustrates hydrogen bond formation between MA and the target proteins throughout the simulation. The PPARα–MA complex maintained between 0 and 4 hydrogen bonds, averaging approximately two bonds. A similar pattern was observed for the PPARγ–MA complex, again averaging around two hydrogen bonds. These results suggest that MA forms stable hydrogen bond interactions with both targets. Additionally, Fig. 7E demonstrates that RMSF values for both PPARα–MA and PPARγ–MA complexes predominantly remained below 3 Å, indicating limited flexibility and high structural stability.

Ligand–receptor binding energies were calculated using the MM/PBSA approach. The binding free energies for the PPARα–MA and PPARγ–MA complexes were –70.317 kJ/mol and –110.574 kJ/mol, respectively. Negative values indicate favorable binding, with lower values reflecting stronger affinities. Thus, MA exhibited a higher binding affinity for PPARγ compared with PPARα. Subsequent analysis identified key amino acid residues critical for ligand binding. In the PPARα–MA complex, residues ARG409, LEU410, LEU408, and GLN413 significantly contributed to binding (**Supplementary Fig. 1A**).

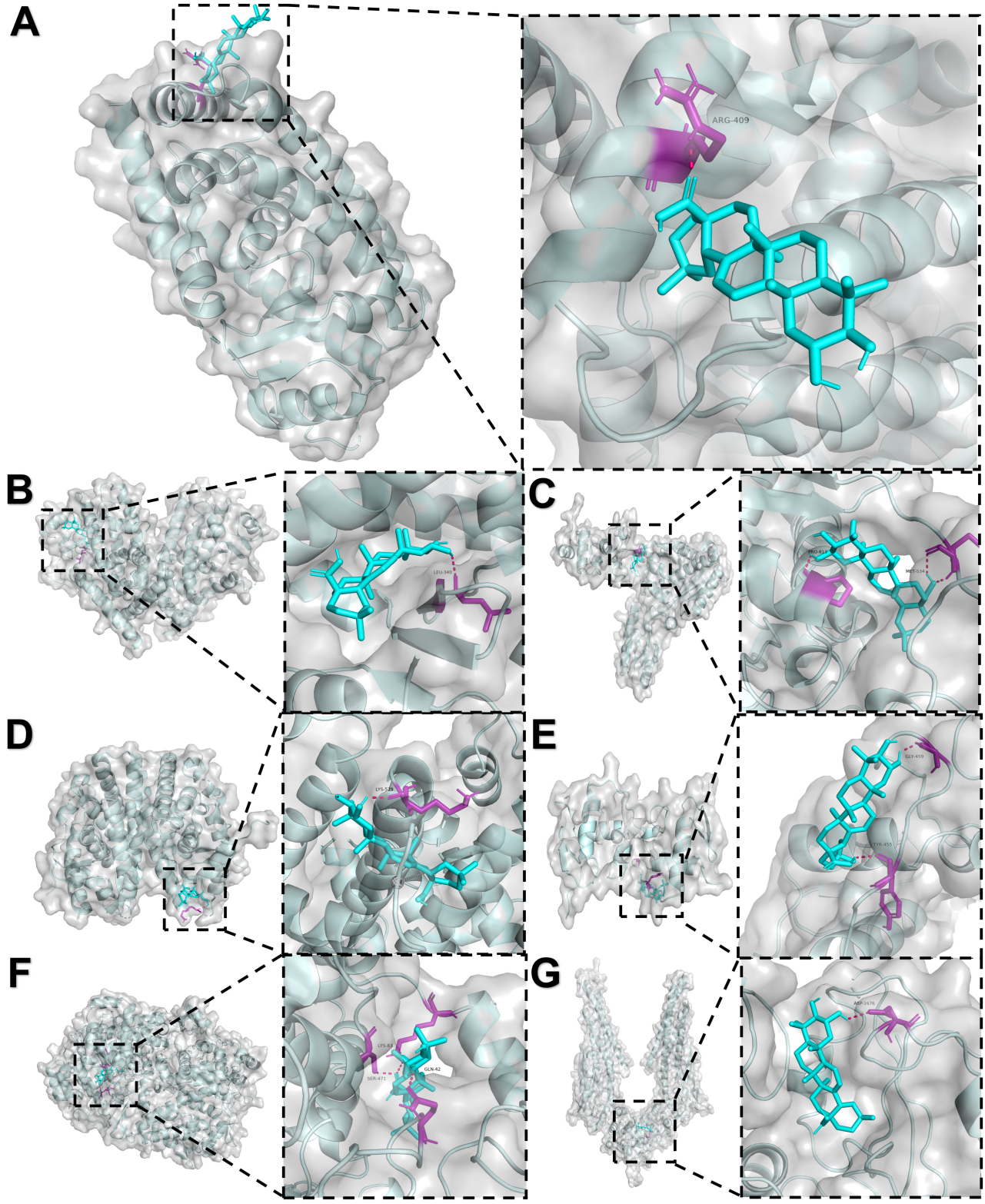

Fig. 6. Molecular docking models depicting interactions between MA and core targets involved in gallstone formation. (A) Peroxisome proliferator-activated receptor alpha (PPARα). (B) Peroxisome proliferator-activated receptor gamma (PPARγ). (C) 3-hydroxy-3-methylglutaryl-CoA reductase (HMGCR). (D) Estrogen receptor 1 (ESR1). (E) Nuclear receptor subfamily 3 group C member 1 (NR3C1). (F) Prostaglandin-endoperoxide synthase 2 (PTGS2). (G) Signal transducer and activator of transcription 3 (STAT3).

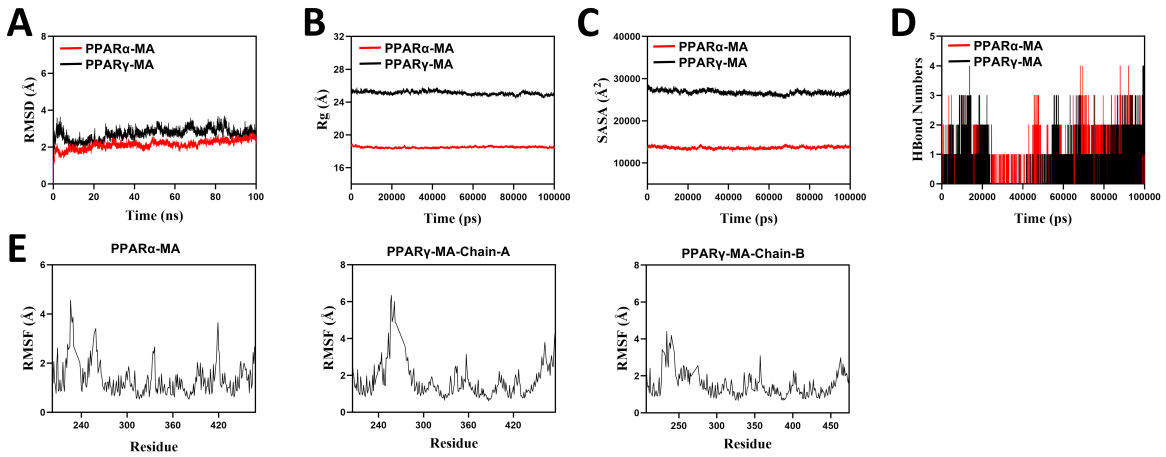

Fig. 7. Molecular dynamics analysis of protein–ligand complexes. (A) Root mean square deviation (RMSD) evolution of complexes over simulation time. (B) Radius of gyration (Rg) indicating structural compactness. (C) SASA dynamics. (D) Temporal patterns of hydrogen bond formation between proteins and MA. (E) Root mean square fluctuation (RMSF) values for protein backbone residues.

In the PPARγ–MA complex, Arg288, Leu255, Cys285, and Lys263 are located in the key positions of the ligand binding pocket and are involved in ligand recognition and binding stabilization (**Supplementary Fig. 1B**), highlighting their potential importance in ligand–protein interactions or catalytic functions. Collectively, these results confirm that MA forms stable complexes with PPARα and PPARγ, exhibiting favorable binding energies and supporting the hypothesis that MA targets PPARα/γ to mediate its biological activities.

Altered Protein Expression of PPAR Signaling Pathway-Related Genes

To investigate the upstream molecular mechanisms by which MA regulates gallstone formation, we examined the expression of key transcription factors in the PPAR signaling pathway. Western blot analysis (Fig. 8) revealed that, compared with the LD group, MA treatment resulted in a significant upregulation of hepatic PPARα protein expression ($p < 0.05$), while simultaneously significantly downregulating PPARγ expression ($p < 0.05$). It has been reported that PPARα agonists, such as fibrates, promote CGS formation by suppressing genes involved in bile acid synthesis [29]. Consistent with our findings, Wang *et al*. [30] reported that inhibition of PPARγ promotes CGS formation in mouse models via dual mechanisms: impaired BA biosynthesis and disruption of enterohepatic circulation. These results suggest that MA may contribute to the pathogenesis of gallstone formation by altering the balance of the PPARα/γ signaling pathway, thereby influencing hepatic lipid and cholesterol metabolism.

Discussion

This study demonstrated that prolonged exposure (4 weeks) to elevated MA doses markedly exacerbated the formation of CGS and induced CLI in mice consuming a cholesterol-rich diet. Mechanistically, MA treatment reduced hepatic expression of critical enzymes responsible for BA synthesis, as well as key transporters involved in BSEP and ABCB4. Collectively, these findings provide robust evidence supporting our initial hypothesis that MA facilitates CGS formation primarily through interference with BA metabolic and secretory pathways.

Moreover, the increased expression of HMGCR, a pivotal enzyme in cholesterol biosynthesis, and decreased expression of PCSK9, a regulator of LDL receptor activity [31], suggest that MA also enhances CGS formation through modulation of cholesterol metabolism. Concurrent downregulation of the drug metabolism-associated protein CYP2B10 results in an exacerbation of hepatic injury.

Histological examination revealed disrupted hepatocyte architecture, pronounced inflammatory cell infiltration, and other pathological features in the MA-H group. It should be noted that the histological presentation focuses on the most severe injury observed in the MA-H group, while the serum biochemical assessment provides a quantitative profile across all treatment doses. These pathological changes, along with the biochemical alterations, provide comprehensive evidence of MA-induced hepatotoxicity.

Through RNA-seq, network pharmacology analysis, MD simulations, and molecular docking, we identified the PPAR signaling pathway as a crucial mediator by which MA promotes CGS formation. Western blot analysis further confirmed the upregulation of PPARα and the downregulation of PPARγ. These findings collectively reinforce our proposed mechanism, wherein MA promotes CGS by perturbing BA homeostasis through the PPAR signaling pathway.

With the growing popularity of herbal medicines globally, herb-induced hepatotoxicity has become a significant clinical concern. However, definitions of hepatotoxic risk

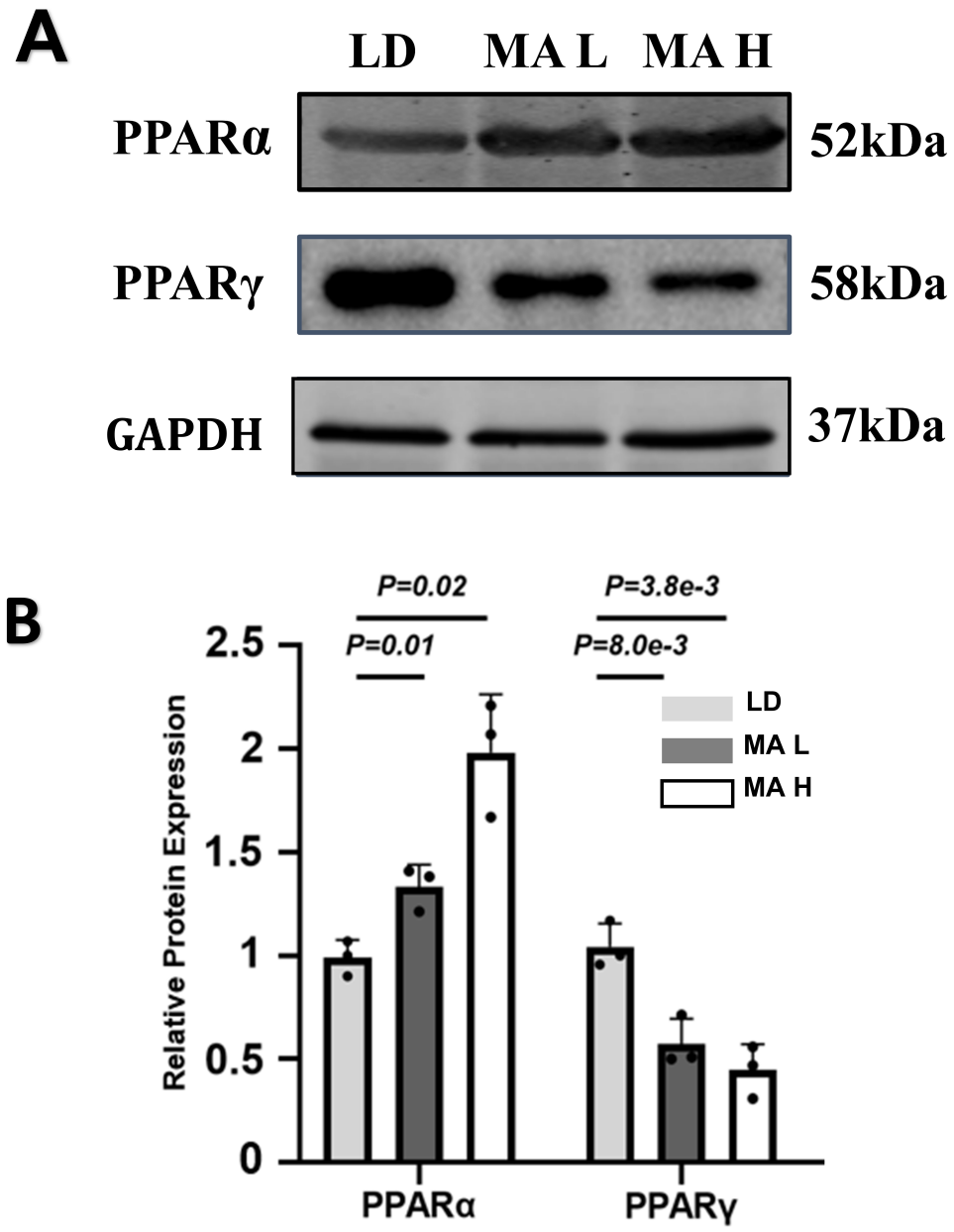

Fig. 8. Protein expression analysis related to signaling pathways. (A) Western blot analysis of liver tissue samples from LD, MA-L, and MA-H groups to assess protein expression of PPARα and PPARγ. (B) Quantitative results of protein expression levels of PPARα and PPARγ. Data are presented as mean ± SEM; n = 3 mice per group. Statistical analysis was performed using one-way ANOVA followed by Tukey's post-hoc test. Exact p-values are indicated in the figure. Comparisons were made relative to the LD group. The LD group served as the baseline control for these mechanistic studies to directly evaluate the effects of MA treatment under gallstone-prone conditions. PPARα, Peroxisome proliferator-activated receptor alpha; PPARγ, Peroxisome proliferator-activated receptor gamma.

remain unclear. Many herbal compounds demonstrating hepatoprotective effects at low doses become hepatotoxic when exceeding certain thresholds—a paradox frequently observed in traditional herbal preparations and bioactive substances [5–7]. Therefore, potential hepatotoxic risks associated with MA should be carefully evaluated alongside its beneficial properties.

According to the Practical Guidelines for the Diagnosis and Early Treatment of Drug-Induced Liver Injury [32], a sustained elevation of ALP levels more than twice the normal upper limit constitutes a clinical criterion for CLI diagnosis. Cholestatic conditions promote the accumulation of BAs within serum and hepatocytes, subsequently provoking inflammatory cascades. BAs, as principal components

of bile fluid, critically facilitate lipid digestion, absorption of fat-soluble vitamins, and regulation of cholesterol homeostasis [33]. Previous research indicates that reductions in hepatic and serum BA levels might represent useful biomarkers predicting the progression of CLI, whereas elevated BA levels within bile may potentially ameliorate hepatotoxicity induced by BA retention [34]. Our findings are consistent with these observations. Moreover, cholestasis is known to promote gallstone formation [15].

Cholestasis also contributes to hepatocyte inflammation. For example, bile acids can directly act as proinflammatory agents, inducing inflammatory cells and inflammatory factors, thereby leading to inflammatory damage [35]. BSEP protein expression is decreased in response to MA. It functions as a bile acid excretion pump within the bile duct [36]. Literature has shown that in cholestatic liver disease caused by abnormalities in the bile salt transporter pump, insufficient BA excretion leads to their accumulation, initially triggering hepatocellular injury and subsequently immune imbalance, inflammation, and fibrosis, which in turn contribute to a secondary wave of damage, further exacerbating cholestatic liver damage [37]. For example, BAs are known to trigger neutrophil-mediated inflammatory responses and can synergize with lipopolysaccharide to promote inflammatory vesicle activation [38]. In this study, significant inflammatory cell infiltration was observed through H&E staining, and inflammatory pathways were enriched by KEGG analysis. Network pharmacology analysis also revealed that the negative regulation of inflammation is a core biological process. These findings are consistent with previous studies.

As an oleanane-type pentacyclic triterpenoid, MA shares structural and functional similarities with oleanolic acid, a recognized PPARα agonist [39]. Our study similarly demonstrated that MA possesses PPARα agonistic activity. Activation of PPARα has been associated with an increased risk of GD. For example, fibrates—well-established PPARα agonists—were first reported by the Coronary Drug Project in 1975 to elevate GD incidence [40]. Other fibrates, such as bezafibrate, fenofibrate, and ciprofibrate, also exhibit lithogenic potential by increasing CSI, similarly to the properties of clofibrate [40]. Furthermore, aligning with our results, it has been reported that PPARα activation correlates with decreased expression of BA synthesis-related genes such as *CYP7A1* and *CYP27A1*, alongside increased expression of the cholesterol synthesis-related gene *HMGCR* [6].

PPARγ is a nuclear receptor activated by specific ligands, critically involved in the regulation of metabolic processes. It forms heterodimers with the retinoid X receptor (RXR), and this complex subsequently interacts with peroxisome proliferator response elements (PPREs) located in target gene promoters. This interaction ultimately influences various biological pathways, including lipid metabolism, adipocyte differentiation, inflammatory responses, and the maintenance of metabolic balance [41]. Notably, activation of PPARγ has been shown to inhibit CGS formation by influencing BA metabolism [30]. This protective mechanism involves upregulating critical enzymes in BA synthesis (CYP7A1 and CYP27A1) as well as the BA transporter BSEP [30], consistent with the findings of our study.

Several limitations of this study should be acknowledged. First, the experiments were conducted in C57BL/6J mice, and thus the findings may not be directly extrapolated to humans; species-specific differences in BA composition and cholesterol metabolism may influence the risk of gallstone formation. Second, although high-dose MA was shown to promote gallstone formation and CLI, the study primarily focused on short-term dietary interventions, and the long-term safety profile of MA remains to be clarified. Third, while transcriptomic analysis, network pharmacology, and molecular docking provided insights into the involvement of the PPAR signaling pathway and BA metabolism, these approaches are predictive in nature, and additional *in vivo* or *in vitro* validation of the precise molecular mechanisms is warranted. Fourth, the study did not explore potential dose–response thresholds or interactions with other dietary and metabolic factors that may modify the risk of gallstone formation. Finally, the conclusions are based on a single animal model and a relatively limited sample size, which may restrict the generalizability of the results. Additionally, for the purpose of focusing on the most pronounced pathological changes and the specific effects of MA within the lithogenic model, representative histological images and Western blot data for the ND group and the MA-L group (in the case of histology) are not presented in the current set of figures. However, the quantitative biochemical and statistical data across all groups that can comprehensively support our conclusions are provided. Future studies incorporating diverse animal models, clinical samples, and long-term evaluations are needed to further substantiate the safety profile of MA and its mechanistic role in CGS formation.

Conclusion

Our study demonstrates that high-dose MA exacerbates CGS formation and induces CLI in C57BL/6 mice on a high-cholesterol diet, primarily through modulation of the PPAR signaling pathway and BA metabolism. These findings elucidate the mechanistic role of MA in promoting CGS formation and highlight key regulatory pathways involved in cholesterol metabolism, BA synthesis, and excretion imbalance, with particular emphasis on PPAR signaling pathway interference. The results not only provide experimental evidence for the toxic risks associated with high-dose MA but also offer new insights into the mechanisms underlying gallstone formation and the potential intervention targets. This research holds significant theoreti-

cal value and contributes to drug safety evaluation as well as the understanding of gallstone formation.

Availability of Data and Materials

The original sequence data reported in this paper have been stored in the Beijing Institute of Genomics, Chinese Academy of Sciences (PRJCA043786), and are publicly accessible. All other data supporting the findings of this study are available from the corresponding authors upon reasonable request.

Author Contributions

SF and ZH led the conceptualization, investigation, and formal analysis, and both authors contributed equally to this work. FH participated in data acquisition and methodology optimization. DL, CS, TL, and HD contributed to sample preparation, data curation, and validation. LL assisted in experimental design and data interpretation. XM contributed to the study conception and design, oversaw data collection, and verified the analyses. XM supervised the project and secured funding together with LL. The manuscript was drafted by SF and FH, and critically revised by all authors for important intellectual content. All authors have approved the final version. All authors have agreed to be accountable for all aspects of the work.

Ethics Approval and Consent to Participate

This research followed all animal welfare protocols established by China's Ministry of Science and Technology (2006 Laboratory Animal Care and Use Guidelines). All animal procedures followed institutional ethical standards and were authorized by the IACUC of The First Affiliated Hospital of Harbin Medical University (Approval No. 2024048), ensuring full compliance with international standards for the humane treatment of laboratory animals.

Acknowledgment

The authors express gratitude to all institutions and individuals who supported this research.

Funding

This work was funded by the National Natural Science Foundation of China (Grant No. 82270598).

Conflict of Interest

The authors declare no conflict of interest.

Supplementary Material

Supplementary material associated with this article can be found, in the online version, at https://doi.org/10.24976/Discov.Med.202537203.243.

References

[1] Liu T, Lv H, Li J, Chen Y, Chen M. Association between dietary fiber intake and gallstone disease in US adults: Data from NHANES 2017-2020. SLAS Technology. 2025; 31: 100259. https://doi.org/10.1016/j.slast.2025.100259.

[2] Shaltout AA, Abd-Elkader OH, Lassen P, Fittschen UA. Elemental Composition of Human Gallstones by Means of TXRF Spectrometry's. X-Ray Spectrometry. 2025; 54: 422–436. https://doi.org/10.1002/xrs.3478.

[3] Calomino N, Poto GE, Carbone L, Bagnacci G, Piccioni S, Andreucci E, *et al*. Neuroendocrine tumors' patients treated with somatostatin analogue could complicate with emergency cholecystectomy. Annali Italiani di Chirurgia. 2023; 94: 518–522.

[4] European Association for the Study of the Liver. EASL Clinical Practice Guidelines: Drug-induced liver injury. Journal of Hepatology. 2019; 70: 1222–1261. https://doi.org/10.1016/j.jhep.2019.02.014.

[5] Yang F, Dong X, Yin X, Wang W, You L, Ni J. *Radix Bupleuri*: A Review of Traditional Uses, Botany, Phytochemistry, Pharmacology, and Toxicology. BioMed Research International. 2017; 2017: 7597596. https://doi.org/10.1155/2017/7597596.

[6] Wang L, Wu G, Wu F, Jiang N, Lin Y. Geniposide attenuates ANIT-induced cholestasis through regulation of transporters and enzymes involved in bile acids homeostasis in rats. Journal of Ethnopharmacology. 2017; 196: 178–185. https://doi.org/10.1016/j.jep.2016.12.022.

[7] Li H, Wang X, Liu Y, Pan D, Wang Y, Yang N, *et al*. Hepatoprotection and hepatotoxicity of Heshouwu, a Chinese medicinal herb: Context of the paradoxical effect. Food and Chemical Toxicology. 2017; 108: 407–418. https://doi.org/10.1016/j.fct.2016.07.035.

[8] Cheng L, Guo M, Farooqi AA, Wang L, Zhang Y, Ye H, *et al*. Interaction between Maslinic acid and HSF1 enhances the ubiquitin degradation of HSF1, resulting in the inhibitory effect of pancreatic cancer. Discover Oncology. 2025; 16: 1069. https://doi.org/10.1007/s12672-025-02786-8.

[9] Yu L, Xie X, Cao X, Chen J, Chen G, Chen Y, *et al*. The Anticancer Potential of Maslinic Acid and Its Derivatives: A Review. Drug Design, Development and Therapy. 2021; 15: 3863–3879. https://doi.org/10.2147/DDDT.S326328.

[10] Yap WH, Lim YM. Mechanistic Perspectives of Maslinic Acid in Targeting Inflammation. Biochemistry Research International. 2015; 2015: 279356. https://doi.org/10.1155/2015/279356.

[11] Moneriz C, Mestres J, Bautista JM, Diez A, Puyet A. Multitargeted activity of maslinic acid as an antimalarial natural compound. The FEBS Journal. 2011; 278: 2951–2961. https://doi.org/10.1111/j.1742-4658.2011.08220.x.

[12] Li T, Wang H, Dong S, Liang M, Ma J, Jiang X, *et al*. Protective effects of maslinic acid on high fat diet-induced liver injury in mice. Life Sciences. 2022; 301: 120634. https://doi.org/10.1016/j.lfs.2022.120634.

[13] Liu J, Lu YF, Wu Q, Xu SF, Shi FG, Klaassen CD. Oleanolic acid reprograms the liver to protect against hepatotoxicants, but is hepatotoxic at high doses. Liver International. 2019; 39: 427–439. https://doi.org/10.1111/liv.13940.

[14] Pass MA, Pugh MW, Findlay L. Studies on the mechanism of toxicity of reduced lantadene A in rats. Biochemical Pharmacology. 1981; 30: 1433–1437. https://doi.org/10.1016/0006-2952(81)90363-4.

[15] Ceci L, Han Y, Krutsinger K, Baiocchi L, Wu N, Kundu D, *et al*. Gallstone and Gallbladder Disease: Biliary Tract and Cholangiopathies. Comprehensive Physiology. 2023; 13: 4909–4943. https://doi.org/10.1002/cphy.c220028.

[16] Sánchez-González M, Lozano-Mena G, Juan ME, García-

Granados A, Planas JM. Assessment of the safety of maslinic acid, a bioactive compound from Olea europaea L. Molecular Nutrition & Food Research. 2013; 57: 339–346. https://doi.org/10.1002/mnfr.201200481.

[17] Gao Q, Bi P, Mi Q, Guan Y, Jiang J, Li X, *et al*. Effect of nicotine on cholesterol gallstone formation in C57BL/6J mice fed on a lithogenic diet. Experimental and Therapeutic Medicine. 2023; 25: 84. https://doi.org/10.3892/etm.2023.11783.

[18] Szklarczyk D, Gable AL, Lyon D, Junge A, Wyder S, Huerta-Cepas J, *et al*. STRING v11: protein-protein association networks with increased coverage, supporting functional discovery in genome-wide experimental datasets. Nucleic Acids Research. 2019; 47: D607–D613. https://doi.org/10.1093/nar/gky1131.

[19] Shannon P, Markiel A, Ozier O, Baliga NS, Wang JT, Ramage D, *et al*. Cytoscape: a software environment for integrated models of biomolecular interaction networks. Genome Research. 2003; 13: 2498–2504. https://doi.org/10.1101/gr.1239303.

[20] Tang Y, Li M, Wang J, Pan Y, Wu FX. CytoNCA: a cytoscape plugin for centrality analysis and evaluation of protein interaction networks. Bio Systems. 2015; 127: 67–72. https://doi.org/10.1016/j.biosystems.2014.11.005.

[21] Mallajosyula SS, Jo S, Im W, MacKerell AD, Jr. Molecular dynamics simulations of glycoproteins using CHARMM. In Lütteke T, Frank M (eds.) Glycoinformatics. Methods in Molecular Biology, vol 1273. Humana Press: New York, NY. https://doi.org/10.1007/978-1-4939-2343-4_25.

[22] Mark P, Nilsson L. Structure and dynamics of the TIP3P, SPC, and SPC/E water models at 298 K. The Journal of Physical Chemistry A. 2001; 105: 9954–9960. https://doi.org/10.1021/jp003020w.

[23] Alimoğulları M, Buluş H. Predictive factors of gallstone formation after sleeve gastrectomy: a multivariate analysis of risk factors. Surgery Today. 2020; 50: 1002–1007. https://doi.org/10.1007/s00595-020-01971-2.

[24] Carey MC. Critical tables for calculating the cholesterol saturation of native bile. Journal of Lipid Research. 1978; 19: 945–955.

[25] Wang Y, Liu K. Therapeutic potential of oleanolic acid in liver diseases. Naunyn-Schmiedeberg's Archives of Pharmacology. 2024; 397: 4537–4554. https://doi.org/10.1007/s00210-024-02959-2.

[26] Sticova E, Jirsa M. ABCB4 disease: Many faces of one gene deficiency. Annals of Hepatology. 2020; 19: 126–133. https://doi.org/10.1016/j.aohep.2019.09.010.

[27] Zhang MY, Wang JP, He K, Xia XM. Bsep expression in hilar cholangiocarcinoma of rat model. Scientific Reports. 2021; 11: 2861. https://doi.org/10.1038/s41598-021-82636-z.

[28] Zhao F, Ma S, Zhou Y, Wei B, Hao Z, Cui X, *et al*. miRNA-223 Suppresses Mouse Gallstone Formation by Targeting Key Transporters in Hepatobiliary Cholesterol Secretion Pathway. International Journal of Biological Sciences. 2021; 17: 4459–4473. https://doi.org/10.7150/ijbs.65485.

[29] Post SM, Duez H, Gervois PP, Staels B, Kuipers F, Princen HM. Fibrates suppress bile acid synthesis via peroxisome proliferator-activated receptor-alpha-mediated downregulation of cholesterol 7alpha-hydroxylase and sterol 27-hydroxylase expression. Arteriosclerosis, Thrombosis, and Vascular Biology. 2001; 21: 1840–1845. https://doi.org/10.1161/hq1101.098228.

[30] Wang G, Han T, Wang S, Chen M, Sun Y, Fu Z. Peroxisome Proliferator-Activated Receptor-γ Prevents Cholesterol Gallstone Formation in C57bl Mice by Regulating Bile Acid Synthesis and Enterohepatic Circulation. BioMed Research International. 2018; 2018: 7475626. https://doi.org/10.1155/2018/7475626.

[31] Lambert G, Sjouke B, Choque B, Kastelein JJP, Hovingh GK. The PCSK9 decade. Journal of Lipid Research. 2012; 53: 2515–2524. https://doi.org/10.1194/jlr.R026658.

[32] Tajiri K, Shimizu Y. Practical guidelines for diagnosis and early management of drug-induced liver injury. World Journal of Gastroenterology. 2008; 14: 6774–6785. https://doi.org/10.3748/wjg.14.6774.

[33] Monte MJ, Fàbrega L, Romero MR, Temprano AG, Kaplowitz N, Garcia-Ruiz C, *et al*. Bile acids in liver and gastrointestinal cancer. Seminars in Cancer Biology. 2025; 116: 45–58. https://doi.org/10.1016/j.semcancer.2025.09.002.

[34] Li WK, Wang GF, Wang TM, Li YY, Li YF, Lu XY, *et al*. Protective effect of herbal medicine Huangqi decoction against chronic cholestatic liver injury by inhibiting bile acid-stimulated inflammation in DDC-induced mice. Phytomedicine. 2019; 62: 152948. https://doi.org/10.1016/j.phymed.2019.152948.

[35] Song M, Chen Z, Qiu R, Zhi T, Xie W, Zhou Y, *et al*. Inhibition of NLRP3-mediated crosstalk between hepatocytes and liver macrophages by geniposidic acid alleviates cholestatic liver inflammatory injury. Redox Biology. 2022; 55: 102404. https://doi.org/10.1016/j.redox.2022.102404.

[36] Marrone J, Danielli M, Gaspari CI, Marinelli RA. Adenovirus-mediated human aquaporin-1 expression in hepatocytes improves lipopolysaccharide-induced cholestasis. IUBMB Life. 2017; 69: 978–984. https://doi.org/10.1002/iub.1689.

[37] Fuchs CD, Paumgartner G, Wahlström A, Schwabl P, Reiberger T, Leditznig N, *et al*. Metabolic preconditioning protects BSEP/ABCB11$^{-/-}$ mice against cholestatic liver injury. Journal of Hepatology. 2017; 66: 95–101. https://doi.org/10.1016/j.jhep.2016.08.017.

[38] Kang H, Liu T, Wang Y, Bai W, Luo Y, Wang J. Neutrophil-macrophage communication via extracellular vesicle transfer promotes itaconate accumulation and ameliorates cytokine storm syndrome. Cellular & Molecular Immunology. 2024; 21: 689–706. https://doi.org/10.1038/s41423-024-01174-6.

[39] Radwan MO, Kadasah SF, Aljubiri SM, Alrefaei AF, El-Maghrabey MH, El Hamd MA, *et al*. Harnessing Oleanolic Acid and Its Derivatives as Modulators of Metabolic Nuclear Receptors. Biomolecules. 2023; 13: 1465. https://doi.org/10.3390/biom13101465.

[40] Clofibrate and niacin in coronary heart disease. JAMA. 1975; 231: 360–381.

[41] Semple RK, Chatterjee VKK, O'Rahilly S. PPAR gamma and human metabolic disease. The Journal of Clinical Investigation. 2006; 116: 581–589. https://doi.org/10.1172/JCI28003.